Design, fabrication, and beam commissioning of a continuous-wave four-rod rf quadrupole

X. J. Yin,[1] Y. J. Yuan,[1] J. W. Xia,[1] Y. He,[1] H. W. Zhao,[1] X. H. Zhang,[1] H. Du,[1] Z. S. Li,[1] X. N. Li,[1] P. Y. Jiang,[1] Y. Q. Yang,[1] L. Z. Ma,[1] J. X. Wu,[1] Z. Xu,[1] L. T. Sun,[1] W. Zhang,[1] X. Z. Zhang,[1] J. Meng,[1] Z. Z. Zhou,[1] Q. G. Yao,[1] G. Z. Cai,[1] W. Lu,[1] H. N. Wang,[1] W. J. Chen,[1] Y. Zhang,[1] X. W. Xu,[1] W. J. Xie,[1] Y. R. Lu,[2] K. Zhu,[2] G. Liu,[2] X. Q. Yan,[2] S. L. Gao,[2] Z. Wang,[2] and J. E. Chen[2]

[1]*Institute of Modern Physics, Chinese Academy of Sciences, Lanzhou 730000, China*
[2]*State Key Laboratory of Nuclear Physics and Technology, Peking University, Beijing 100871, China*
(Received 22 May 2015; published 22 January 2016)

A new heavy-ion linac within a continuous-wave (CW) 4-rod radio-frequency quadrupole (RFQ) was designed and constructed as the injector for the separated-sector cyclotron (SSC) at the Heavy Ion Research Facility at Lanzhou (HIRFL). In this paper, we present the development of and the beam commissioning results for the 53.667 MHz CW RFQ. In the beam dynamics design, the transverse phase advance at zero current, $\sigma_{0\perp}$, is maintained at a relatively high level compared with the longitudinal phase advance ($\sigma_{0\parallel}$) to avoid parametric resonance. A quasi-equipartitioning design strategy was applied to control the emittance growth and beam loss. The installation error of the electrodes was checked using a FARO 3D measurement arm during the manufacturing procedure. This method represents a new approach to measuring the position shifts of electrodes in a laboratory environment and provides information regarding the manufacturing quality. The experimental results of rf measurements exhibited general agreement with the simulation results obtained using CST code. During on-line beam testing of the RFQ, two kinds of ion beams ($^{40}Ar^{8+}$ and $^{16}O^{5+}$) were transported and accelerated to 142.8 keV/u, respectively. These results demonstrate that the SSC-Linac has made a significant progress. And the design scheme and technology experiences developed in this work can be applied to other future CW RFQs.

DOI: 10.1103/PhysRevAccelBeams.19.010402

I. INTRODUCTION

The HIRFL accelerator complex was upgraded with a multifunctional cooler storage ring (CSR) at the end of 2007 [1]. The injector of the CSR consists of one ion source and two cyclotrons, namely, a sector-focusing cyclotron (SFC) and SSC. The light-ion beams coming from the SFC with an energy of 5.62 MeV/u can be injected directly into the CSR for various experiments, such as precise mass measurement experiments, single-particle-event tests, atomic experiments, and cancer therapy research. The heavy ions also coming from the SFC must be first injected into the SSC, accelerated to 10.06 MeV/u, and then transported into the CSR. However, this operating scheme results in low beam efficiency, especially for heavy ions [2]. To improve the operating status of the apparatus, a linac injector named the SSC-Linac has been proposed as an injector for the SSC. The SSC-Linac mainly consists of a superconducting high-charge-state electron cyclotron resonance (ECR) ion source, a low energy beam transport (LEBT) section including a chopper and a multiharmonic buncher (MHB), a CW RFQ, a medium energy beam transport (MEBT) section, four IH-DTL cavities and a high energy beam transport (HEBT) section [3], as shown in Fig. 1.

The SSC-Linac RFQ, which operates in CW mode to match the operation of the SSC, can accelerate particles with charge-to-mass ratios between 1/3–1/7 from 3.728 keV/u to 143 keV/u. As designed, this machine will transport $^{238}U^{34+}$ beams at a current of 0.5 pmA. This is a very intense beam for such high-charge-state heavy ions. Thus a wide safety margin would be preferable for different ion species and beam intensities because the high charge state will enhance the space charge force. These requirements pose challenges not only in the beam dynamics but also in the design of the cooling of the structure and in ensuring stable long-term operation. Several strategies, such as a specialized match design method, have been applied in the process of designing the CW RFQ [4].

In this paper, the design and commissioning of SSC-Linac RFQ is reported. The detail of the design scheme is described in Sec. II. In Sec. III, the fabrication procedure and low-power rf measurement is presented. The high power conditioning and beam commissioning results are shown in Sec. IV. Finally, the summary of the paper is given in Sec. V.

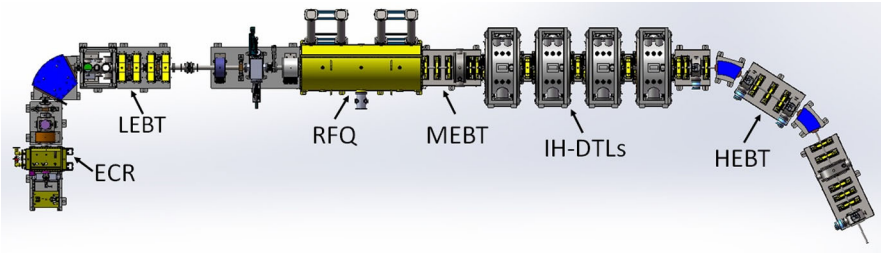

FIG. 1. The general layout of the SSC-Linac.

II. DESIGN AND SIMULATION

Compared with pulsed machines, the number of CW RFQs that have been successfully designed and are currently in operation throughout the world is very limited [5]. The main difficulty facing CW RFQs is the ability to ensure stable long-term operation, including the control of particle loss. Thus, an appropriate design strategy should efficiently minimize the emittance growth and control the beam loss. In our approach, we adopted a very careful design and fabrication procedure. An interactive and iterative process was implemented among the different stages of R&D for the RFQ, namely, the electromagnetic design, the beam dynamics simulations, fabrication, and manufacture.

A. Beam dynamics design

In our beam dynamics design, the desired acceleration, the minimum vane length, the maximum transmission efficiency, the desired energy and the phase widths were regarded as the main concerns, just similar as conventional design. The widely used code PARMTEQM [6] was adopted to perform the beam dynamics simulations. Meanwhile, the transverse phase advance was aptly increased and kept relatively high to avoid parametric resonance. The equipartitioning (EP) strategy has been also applied in the design for controlling the emittance growth and beam loss.

For a qualitative analysis in light of the physics involved, we can rewrite the expression for the radial focusing parameter [7]. According to the theory of RFQ beam dynamics, the radial focusing parameter B [8] is given by

$$B = \frac{q\lambda^2 XV}{mc^2 a^2} \tag{1}$$

where q is the charge state of the ions, λ is the RF wavelength, X is the focusing parameter, V is the intervane voltage, m is the rest mass of the ion, c is the velocity of light in vacuum, and a is the aperture radius of the RFQ. Furthermore, Eq. (1) can be rewritten in terms of the RFQ working frequency $f = c/\lambda$ and the charge-to-mass ratio $\eta = q/m$ of the design ion to be accelerated as follows:

$$B = \left(\frac{1}{f}\right)^2 \frac{\eta XV}{a^2} \tag{2}$$

In this form, the effects of the relations among the parameters B, f, X, V, η and a are more evident. For the design ion of the RFQ, η and f are invariant. Thus, only X, V and a can determine B. From an analysis of the particle motion equation in the RFQ field, we can obtain the phase advance at zero current via several transformations as follows:

$$\sigma_{0\perp}^2 = \frac{1}{2}(B/2\pi)^2 + \Delta_{rf} \tag{3}$$

$$\sigma_{0\parallel}^2 = \frac{\pi^2 qAV|\sin\phi_s|}{mc^2\beta_s^2} \tag{4}$$

where $\Delta_{\mathrm{rf}} = \frac{\pi^2 qAV\sin\varphi_s}{2mc^2\beta^2}$ is the rf defocusing factor [9]. Furthermore, Δ_{rf} can also be expressed as

$$\Delta_{\mathrm{rf}} = -\frac{1}{2}\sigma_{0\parallel}^2 \tag{5}$$

By substituting Eq. (5) into Eq. (3) and performing transformation, we can obtain a new expression relating the transverse and longitudinal phase advances at zero current:

$$\sigma_{0\parallel}^2 + 2\sigma_{0\perp}^2 = (B/2\pi)^2 \tag{6}$$

This equation clearly shows that $\sigma_{0\perp}$ and $\sigma_{0\parallel}$ are coupled with each other. In practice, the conventional design method requires that the radial focusing strength B must remain almost constant along the RFQ [7,10]. Thus, Eq. (6) reduces to

$$\sigma_{0\parallel}^2 + 2\sigma_{0\perp}^2 \cong \text{Constant} \tag{7}$$

Furthermore, from Eq. (4), one can obtain

$$\sigma_{0\parallel}^2 \propto |\phi_s| \tag{8}$$

Thus, the transverse phase advance $\sigma_{0\perp}$ will correspondingly decrease to maintain a constant B, according to Eq. (7). As reported in Ref. [11], the strongest resonance occurs when $\sigma_{0\perp} = \frac{1}{2}\sigma_{0\parallel}$. In practice, a parametric

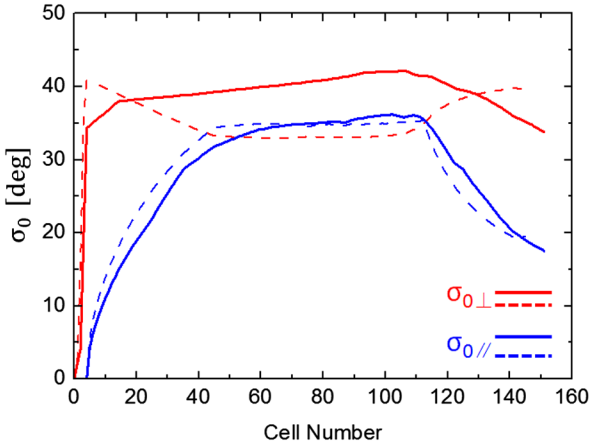

FIG. 2. The evolution of the phase advance at zero current.

resonance, such as $\sigma_{0\perp} = \sigma_{0\parallel}$, will also exist. This phenomenon has been confirmed in our design. Figure 2 shows the evolution of the phase advance at zero current of SSC-Linac RFQ in the transverse plane ($\sigma_{0\perp}$) and the longitudinal plane ($\sigma_{0\parallel}$). The dashed curves in Fig. 2 represent the calculation results before optimization using the conventional design strategy. The longitudinal phase advance $\sigma_{0\parallel}$ is observed to increase sharply since the longitudinal accelerating field grows to supply the bunching force in the shaper section (SP). During the same process, the transverse phase advance $\sigma_{0\perp}$ decrease. In the subsequent section, $\sigma_{0\parallel}$ becomes nearly the same as or even equal to $\sigma_{0\perp}$. They come close at the position of the 40 cell and keep almost constant in the gentle buncher section (GB). As a result, parametric resonance will be induced, and the beam emittance will increase considerably. This emittance enhancement is not a serious problem in the low-current case; however, in the high-current case, it will lead to severe particle loss. Thus, the $\sigma_{0\perp} = \sigma_{0\parallel}$ resonance condition should be avoided in the design.

To resolve these problems, we applied an improved design strategy. The conventional strategy of increasing the longitudinal focusing strength was still adopted, leading to an increase in $\sigma_{0\parallel}$. At the same time, $\sigma_{0\perp}$ was increased by increasing the transverse focusing strength to keep the balance of the focusing force and defocusing effect caused by the space charge force. To avoid parametric resonance, $\sigma_{0\perp}$ was maintained at a relatively high level, causing the transverse phase advance with current to remain stable to satisfy the matching condition, thereby limiting the emittance growth. The solid lines in Fig. 2 represent the values of $\sigma_{0\perp}$ and $\sigma_{0\parallel}$ after optimization. It clearly shows that $\sigma_{0\perp}$ and $\sigma_{0\parallel}$ have been effectively separated. This design strategy avoids the parameter resonance at $\sigma_{0\perp} = \sigma_{0\parallel}$, as described above. At the same time, it enhances the transverse focusing strength while the beam is bunched in the longitudinal plane.

The normalized RMS emittance of the designs before and after optimization are compared as shown in Fig. 3. As can be seen in Fig. 3(a), the emittance in the transverse plane increases significantly during the bunching process because of parametric resonance, and it remains at a high level through tens of cells. The maximum value is 0.25π mm mrad at the 50th cell. The longitudinal emittance remains lower than 6π keV/u ns prior to the 100th cell. However, at the end of the GB, the longitudinal emittance increases considerably and reaches a maximum of 13π keV/u ns at the 125th cell. The coupling and nonlinear effect cause the transverse emittance to simultaneously decline after the 100th cell. Because of the loss of nonsynchronous particles at the entrance to the acceleration section (ACC), the longitudinal emittance rapidly decreases. By contrast, in Fig. 3(b), the RMS emittance values in the transverse plane remain approximately in the range of 0.2–0.23π mm mrad. In particular, in the longitudinal plane, the RMS emittance clearly decreases compared with that shown in Fig. 3(a). The maximum value is only 6π keV/u ns.

The quasi-equipartitioning (EP) design as another design strategy was applied to account for the space charge effect. This EP strategy has been proposed for rf linac design as an effective solution for controlling emittance growth, halo formation and beam loss [12]. As described above, for a $^{238}U^{34+}$ beam at a current of 0.5 pmA, the space charge effect will not be negligible. Thus, EP design is a good strategy for the high-current case.

Both of the phase advances at nonzero current, $\sigma_\perp$ in the transverse plane and $\sigma_\parallel$ in the longitudinal plane, can be described as follows [13]:

$$\sigma_\perp^2 = \sigma_{0\perp}^2 - \Delta_{\perp sc} \tag{9}$$

$$\sigma_\parallel^2 = -(\sigma_{0\parallel}^2 + \Delta_{\parallel sc}) \tag{10}$$

where $\Delta_{\perp sc} = I\lambda^3\ k(1-g)/(\gamma^3 r_a^2 r_b^2)$ and $\Delta_{\parallel sc} = 2I\lambda^3\ kg/(\gamma^3 r_a^2 r_b^2)$ are the space charge defocusing factors in the transverse and longitudinal planes, respectively; r_a and r_b are the transverse and longitudinal RMS beam radii, respectively; g is the ellipsoidal geometry factor and

$$k = (3\pi/8)\left(\frac{Z_0 qe}{mc^2}\right) \tag{11}$$

where $Z_0 = 376.73\ \Omega$ is the impedance of free-space.

In the RFQ, the longitudinal beam length r_b decreases in the SP section because of the strengthening of the phase oscillation, causing $\Delta_{\perp sc}$ to increase and $\sigma_\perp$ to become even smaller in Eq. (9). As a consequence, a mismatch will arise in the beam, which will also cause transverse emittance growth [14]. Thus, the design strategy should be improved to control the beam loss and to minimize emittance growth.

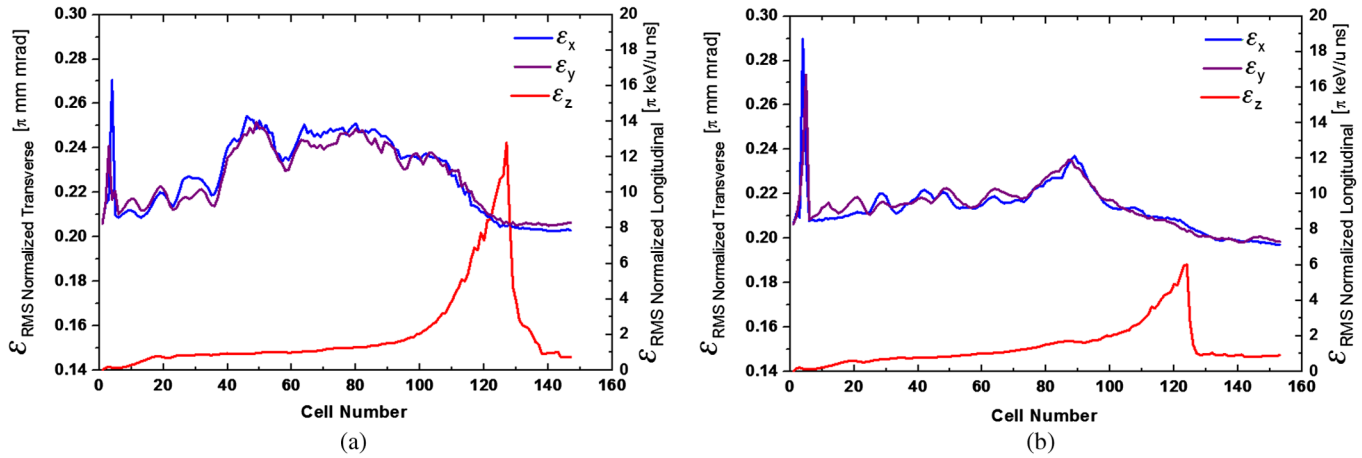

FIG. 3. The normalized RMS emittances of the designs before (a) and after (b) optimization.

The EP condition means no free energy transfer between transverse and longitudinal degrees of freedom, which will make the design more stable. The optimized method is to adjust the transverse phase advance $\sigma_\perp$ to confine the variation of beam size and emittance.

Assuming that there is an ellipsoidal bunched beam in the GB and ACC sections within matched beam radii r_a and r_b, the phase advances with current are related to emittances which obey the following equipartitions:

$$\varepsilon_\perp = \frac{r_a^2 \gamma \sigma_\perp}{\lambda} \tag{12}$$

$$\varepsilon_\parallel = \frac{r_b^2 \gamma^3 \sigma_\parallel}{\lambda} \tag{13}$$

Then, the beam will be in equilibrium and will follow the equipartition condition

$$T = \frac{\varepsilon_\perp \sigma_\perp}{\varepsilon_\parallel \sigma_\parallel} \tag{14}$$

When $T = 1$, the beam can be said to be in the equipartitioned state [15].

In the RFQ design scheme of EP, four variable parameters, m, a, ϕ_s and V, can be used to confine the beam to keep matching and EP condition in the whole bunching and accelerating process as functions of cell number. Since the intervane voltage V is constant, so m, a and ϕ_s are used in practical to satisfy the EP conditions. For the EP condition, m can be determined by solving the equations (12), (13), and (14) for beam radii r_a and r_b simultaneously. Figure 4 presents the cell parameters of SSC-Linac RFQ applying EP condition. In our design, the excess parameters were specified initially: $\varepsilon_\perp$ was assumed as 0.206π mm mrad, $\varepsilon_\parallel/\varepsilon_\perp$ was set to be 1.2 (in GB/ACC section). The intervane voltage V is fixed at 70 kV.

As can be found in Fig. 4, at the entrance of the radial matching section (RMS), the synchronous phase is maintained at a large value $\sim -90°$ to obtain the high capture efficiency. At the beginning of the SP (~5 cell) section, the transverse energy of input beam is much larger than its longitudinal energy. The beam is not in equilibrium and it is

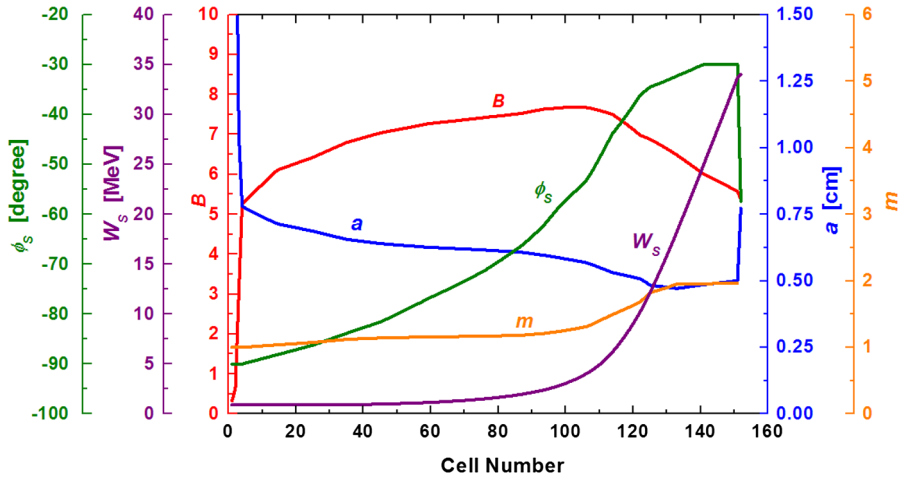

FIG. 4. The cell parameters of SSC_Linac RFQ.

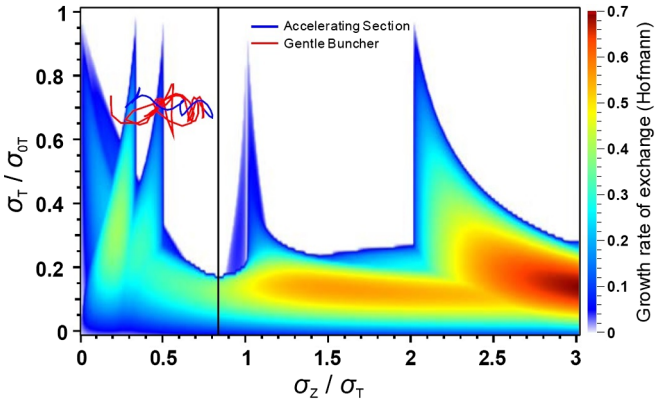

FIG. 5. The footprints of the RFQ phase advance.

also gradually compressed by a longitudinal field, which increases steadily from zero. The synchronous phase at the end of the SP requires us to be far enough from −90° to provide adequate longitudinal focusing for the EP condition. Then the rf defocusing parameter $|\Delta_{rf}|$ increases gradually until arriving at the starting point in GB (∼30 cell) section. The modulation factor m is gradually increased during this procedure. Thus, the aperture radius a decrease relatively fast from the entrance, which leads to the focusing parameter B also increasing to keep the balance of the free energy between the transverse and longitudinal planes. In the GB (30–125 cell) and ACC (125–152 cell) sections, the longitudinal focusing increases steadily as ϕ_s increase to −30°. Then m also keeps increasing steadily and a decreases continuously. Thus the transverse focusing strength B increases and maintains at high level to balance the longitudinal force. As can be seen, at the end of the GB (∼110 cell), the longitudinal focusing force get weaker. Then the transverse focusing B also could be decreased for balance consideration. This procedure results in a rapid decrease of the RFQ aperture in the end of GB section as long as the modulation is increased. The beam loss tends to occur near the choke point as shown in Fig. 3. To avoid it, the beam radius and aperture of the accelerator will be enlarged very slowly before the choke point, the phase advance $\sigma_\perp$ will slowly decreased following Eqs. (9), (10), (12), (13). In the ACC section, longitudinal space-charge effect decreases furthermore, then the B is also decreased for maintaining EP condition. Both m and a keep quasiconstant until the end of the ACC section.

The Hofmann chart [16,17] serves as a valuable guide for the equipartitioning design strategy for controlling the emittance growth and beam loss in a hadron linac. Figure 5 shows the footprints of our RFQ phase advance in the Hofmann chart. In the GB section, the footprint predominantly remains between two resonance peaks, indicating that the beam maintains its equipartitioned state. However, in the ACC section, the beam leaves the equipartitioned state because the longitudinal phase advance decreases rapidly. As also can be found in Fig. 5, the footprints in the GB and ACC sections experience some resonance areas, but these areas in the Hofmann chart are weaker resonance areas. Since the beam was transported through the cavity in the linac only once, these experiences occur also only one times. Thus the coupling between transverse and longitudinal planes has a weak effect on the rms emittance growth [18].

In our design procedure, the beam dynamics simulations were iteratively performed using the TRACK code [19]. The full 3D field distribution was exported from the calculation result as a single cavity [20] of the CST Microwave Studio [21] and input into the TRACK code. Figure 6 shows the results of the TRACK simulations, which are in agreement with the beam dynamics simulations performed using PARMTEQM.

The main parameters of the SSC-Linac RFQ are listed in Table I. For an output energy of approximately 143 keV/u, the required intervane voltage is 70 kV, which is approximately 1.523 times the Kilpatrick limit at 53.667 MHz.

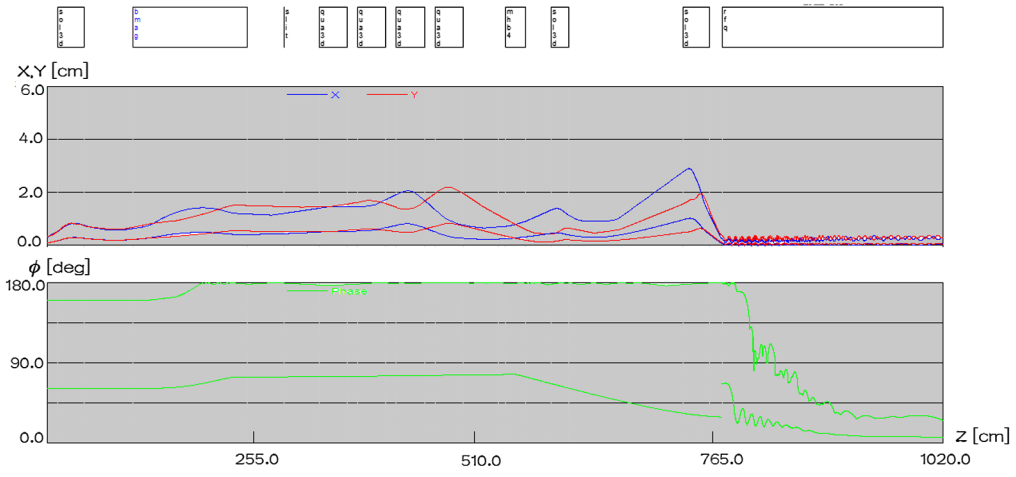

FIG. 6. The evolution of the beam envelope throughout the SSC-Linac front-end section.

TABLE I. Main Parameters of the SSC-Linac RFQ.

Parameter	Value
Frequency [MHz]	53.667
Design ions	$^{238}U^{34+}$
Charge-to-mass ratio	1/7
Beam current [pmA]	0.5
Input energy [keV/u]	3.728
Output energy [keV/u]	143
Duty factor	100%
Intervane voltage V [kV]	70
Synchronous phase φ_S	$-90°$– $-30°$
Power consumption [kW]	30
Minimum aperture a [cm]	0.472
Maximum modulation factor m	1.94
Transmission efficiency	94.1%
Vane length [cm]	250.846

B. Rf structure design

Our studies of the rf structure focused on three aspects: the distribution of the electric field that satisfies the beam dynamics requirements, the power consumption in the rf structure, and the thermal deformation of the structure combined with the cooling channel design. Figure 7 presents the RFQ structure model created using CST Microwave Studio CST.

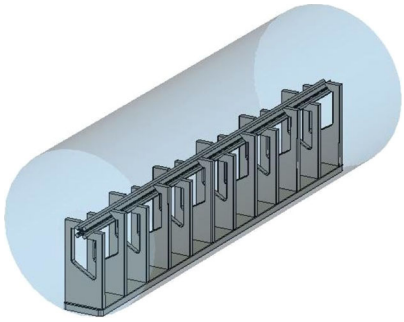

FIG. 7. RFQ cavity model in the CST simulation.

1. General characteristics of the rf design

In the ideal case, the inter-vane voltage should be as flat as possible. However, it is very difficult to fulfill this requirement because of the modulation and the manufacturing error.

In a 4-rod RFQ, the electrode modulation of the quadrupole forms the longitudinal component of the electric field, while it also makes the capacitance between the electrodes to be inhomogeneous. Consequently, the field distribution will show fluctuations. Other factors, such as the end flanges, also affect the field distribution. In addition, the relation between the field distribution and the intervane voltage should be determined through the rf measurements. The calculated capacitance between our RFQ electrodes is shown in Fig. 8 by the red curve. The inhomogeneous distribution of the voltage between the electrodes will cause a nonflat field. Furthermore, this unflatness will influence the beam dynamics if it exceeds a certain limit. In our case, error analysis indicates that an intervane voltage tolerance of below 3% is sufficient for the beam dynamics requirements. Therefore, the quality of the electric field in the RFQ should be verified.

2. Theoretical analysis of the field flatness and the dipole component of the field

Two critical features, the flatness of the quadrupole field and the component of the dipole field, are of concern for the designer of an RFQ structure. The former is represented by the local deviation of the field relative to its average level. The latter is the intrinsic dipole field of the 4-rod asymmetric structure, which is related to the difference in the level of the field between quadrants I and III, as shown in Fig. 9.

In fact, the field can be measured, but the distribution of the intervane voltage cannot be measured directly. Therefore, the distribution relation between the intervane voltage and the field flatness along the electrode should be determined. Thus, we should seek a measurement position

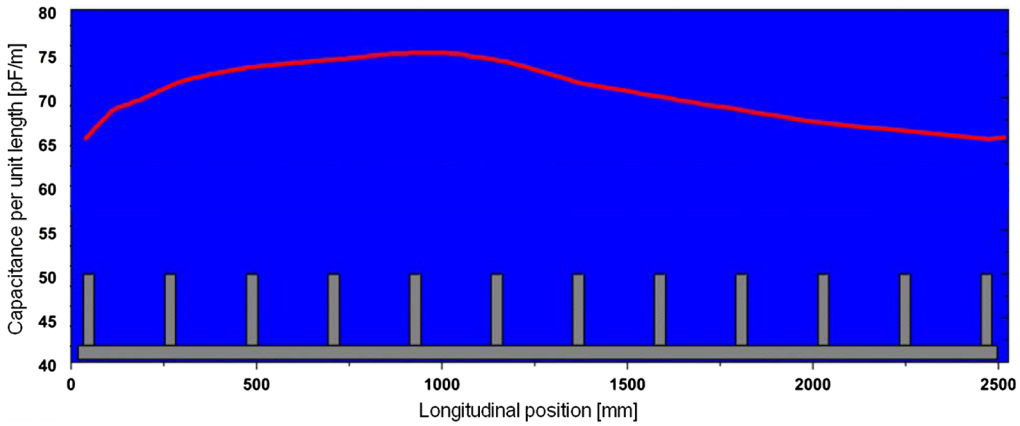

FIG. 8. The calculated capacitance between RFQ electrodes.

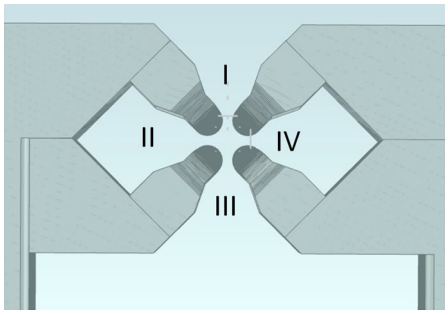

FIG. 9. A cross-sectional view of each quadrant in the RFQ.

on the transverse plane where the field distribution is the same as the intervane voltage distribution.

Figure 10(a, b, c) presents the calculated results of the field distribution and the inter-vane voltage distribution at the transverse position of 10 mm, 15 mm and 20 mm from beam axis, respectively. It can be clearly found that both the field distributions at 10 mm [Fig. 10(a)] and at 15 mm [Fig. 10(b)] have large discrepancies from the intervane voltage distributions. However, the agreement was satisfied at the transverse position of 20 mm. As shown in Fig. 10(c), the field distribution is consistent with the intervane voltage along the RFQ at quadrant I. Thus, the set of results obtained at the corresponding 20 mm displacements can be representative of the final design values for the field flatness in each quadrant; these results are presented in Fig. 10(d) and lie in the range of $\leq \pm 2.5\%$.

As mentioned above, the dipole field component is the intrinsic dipole field of the 4-rod asymmetric structure. This field component will act as a continuous kick on the particles, which will cause the beam center to shift and eventually lead to beam loss. Thus, the dipole field component should be minimized and controlled within a reasonable range. Because the 4-rod RFQ has an asymmetric structure in quadrants I and III, as illustrated

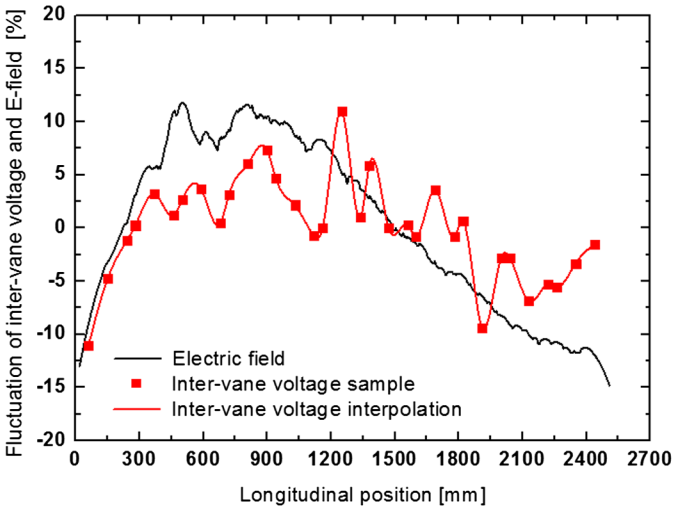

(a)

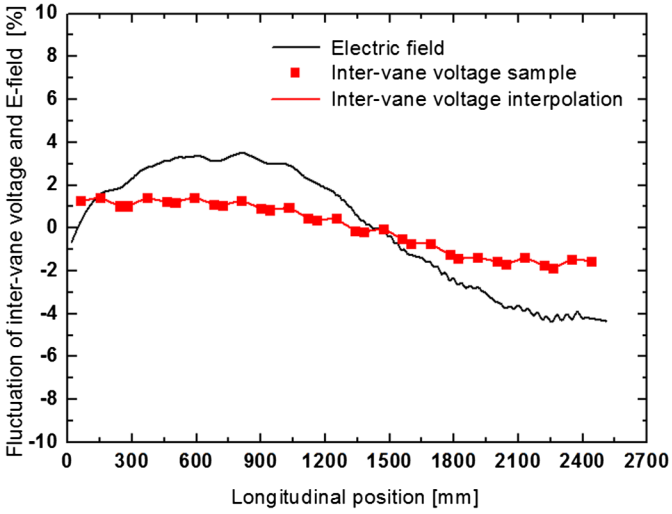

(b)

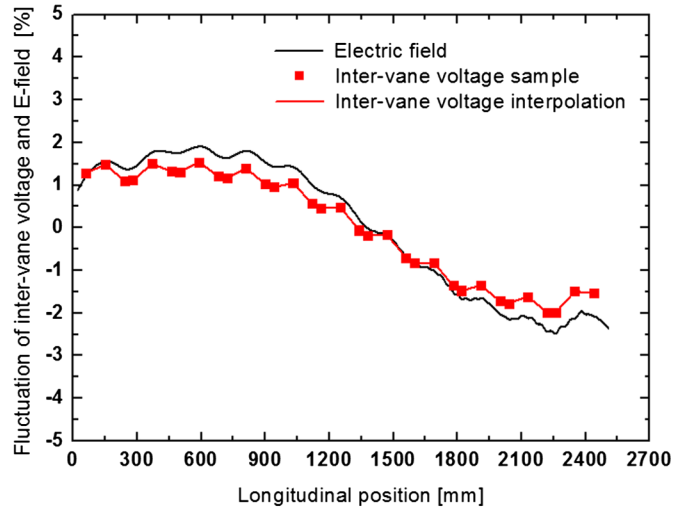

(c)

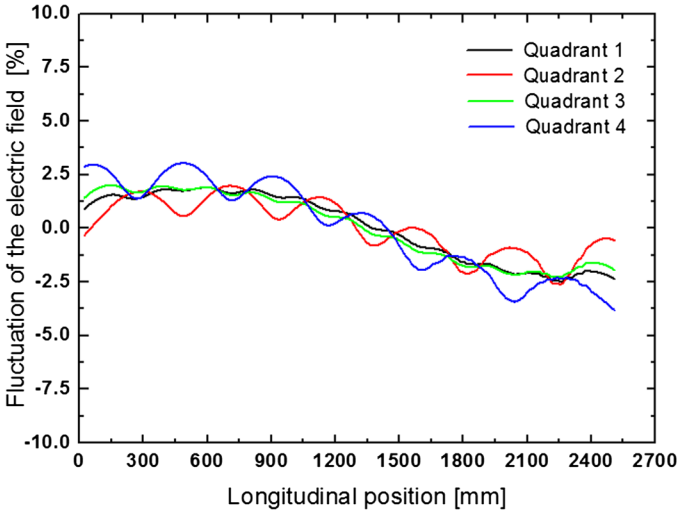

(d)

FIG. 10. The simulated field flatness at various transverse positions.

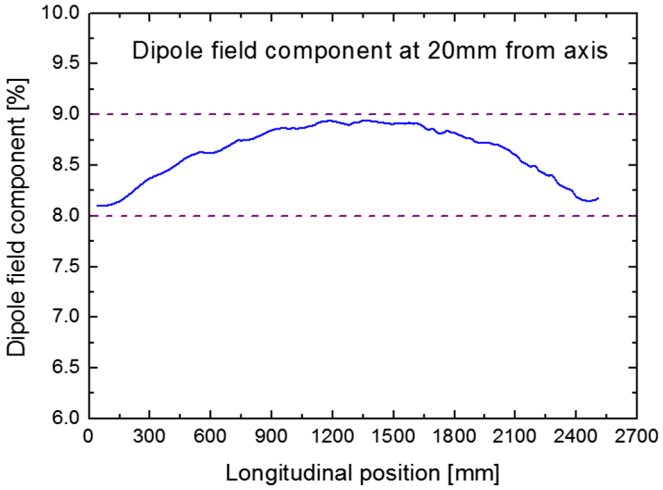

FIG. 11. The dipole field component at a transverse position of 20 mm according to the simulation.

in Fig. 9, the dipole components can be described as follows:

$$\delta_{\text{dipole}\,i} = \frac{E_{1,i} - E_{3,i}}{E_{3,i}} \tag{15}$$

Here, $E_{1,i}$ and $E_{3,i}$ are the electric fields in quadrants I and III, respectively, at the same position i in both the transverse and longitudinal planes along the electrode. By combining the results of our investigation of the field flatness, we find that the dipole components are in the range of 8%-9% at distances of 20 mm from the beam axis in all four quadrants, as shown in Fig. 11.

C. Power consumption and cooling design

Studies of the magnetic energy density and the power consumption distribution can provide background for the cooling design, which is important to ensure reliable operation in CW mode. Figure 12 shows the simulated results for the distributions of the magnetic energy density on the rf structure and the temperature distribution with cooling systems for an input power of 35 kW. As seen in Fig. 12(a), the energy density was mainly consumed on the stem and electrodes. The highest energy density, which occurs in the second stem from the entrance of RFQ, is 74.4 J/m^3.

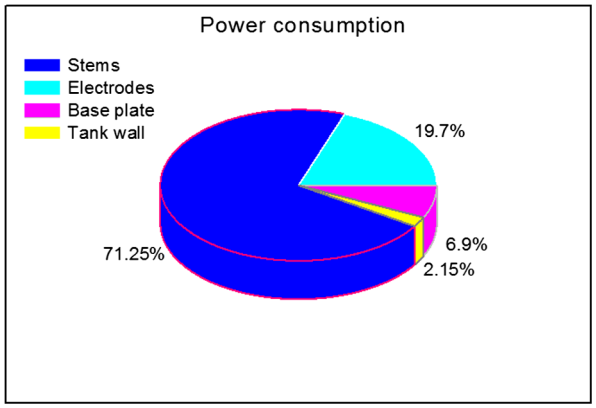

FIG. 13. Power consumption in the RFQ structure.

The power consumptions for each section were also calculated and the results are presented in Fig. 13. More than 90% of the power consumption is dissipated in the stems and electrodes. Thus, care should be taken with the cooling channel design for the stems and electrodes.

In the traditional design for a pulsed machine, there is only one cooling channel, which is primarily used for stem cooling. However, this design is not sufficient for a CW machine. Thus, we created a design with two loops in the end stem. Figure 14 shows the cooling design for the stems. One loop, channel 1, is the main cooling channel in the stem, as in the typical design. A second cooling channel, channel 2, is used to cool the electrode and also to cool the stem. Figure 12(b) presents the temperature distribution achieved when this cooling design is implemented. The maximum temperature increase is only 29 °C. The thermal deformation caused by the power consumption was also analyzed. The maximum deformation was found to be 81.1 μm in the middle section of the electrode. With further study, we found that the deformation of the electrodes is primarily caused by the deformation of the stem tops, where the connection joints between the stems and the electrodes are located. The contribution of the thermal effect on the electrodes themselves to this deformation is less significant.

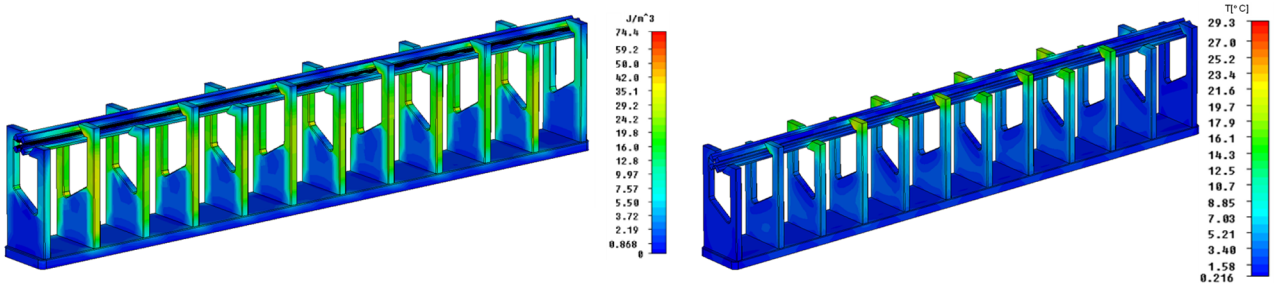

(a) (b)

FIG. 12. Temperature distributions on the rf structure without and with the cooling system.

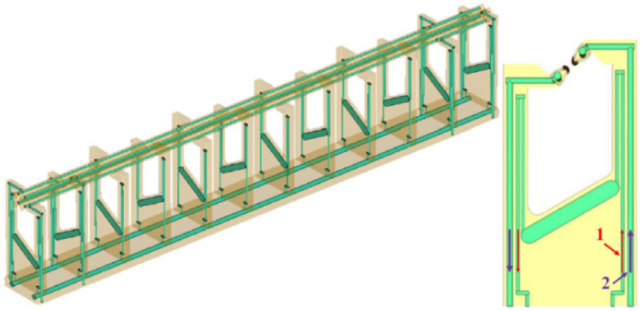

FIG. 14. Cooling channel design in the stems.

III. FABRICATION AND RF MEASUREMENTS

A. Manufacture and assembly

The electrodes, stems and base plate in the RFQ structure were fabricated from 99.97% OFE copper. The inner surface of the RFQ cavity is an electroformed copper plate. All four electrodes for the RFQ were manufactured with high accuracy by a numerical control manufacturing center. During the manufacturing process, the accuracy of the machining of the vane tips was confirmed using the coordinate measuring machine (CMM) in the factory. An inner view of the RFQ is shown in Fig. 15.

The assembly of the electrodes was performed on the numerically controlled three-dimensional CMM. The assembly bases, which also were manufactured with high accuracy along with the electrodes, were treated as the basis for alignment during the assembly. Four screws made of electroformed silver were fastened between the base and the stem each joint section, as shown in Fig. 15. Each opposing pair of electrodes was directly supported by six stems. A total of 12 stems were mounted on the base plate via welding.

All of the attached instruments, including 4 moveable tuners, 1 rf coupler, 2 pickup loops, and 3 turbo pumps, were installed. The 2 pickup loops were identical and were calibrated to the same loss order. In the rf conditioning stage, a solid-state CW 60 kW rf amplifier will supply the rf power to the RFQ through the rf couplers.

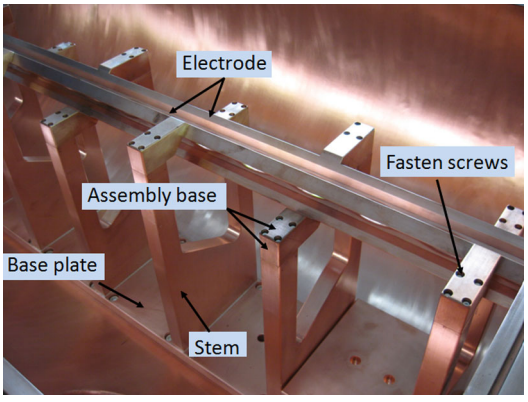

FIG. 15. An inner view of the RFQ structure.

B. Mechanical measurements

As mentioned above, the electrodes are connected to the stems with screws. The various factors influencing the positions of the rods include the installation accuracy, vibrations during shipping, and thermal deformation, among others. The RFQ was transported from the workshop in Shanghai to IMP in Lanzhou via truck over a shipping distance of almost 2200 km. The connection points between the electrodes and stems experienced considerable vibration during this time. These vibrations distorted the positions of the electrodes, potentially influencing the electric field distribution. A similar position shift was observed in the electrovane of the EBIS RFQ cavity at Brookhaven National Laboratory (BNL) [22]. In addition, the power consumption would increase if the connections between sections were loose, as indicated in the analysis presented in Sec. II B. Therefore, before the low power rf measurements, it was necessary to carefully check the positions of the electrodes and realign them in the case of any large shifts.

For this purpose, we introduced a combined method using a laser tracker (Leica AT401) and an articulated arm (FARO) for a mechanical survey of the RFQ (as shown in Fig. 16). The accuracies of the laser tracker and the articulated arm were ± 0.03 mm and ± 0.02 mm, respectively. Before the measurement, the environmental coordinate system was established by the laser tracker based on several fiducial points that had previously been fixed at various locations in the laboratory. The beam axis was simultaneously determined using this system. In this coordinate system, the articulated arm was used to measure the surfaces and positions of the electrodes. This combined application of two types of high-accuracy instruments enabled efficient, highly accurate measurements.

Figure 17 shows the measurement planes and the measured results. Two side surfaces of each electrode were measured, as shown in Fig. 17(a). The deviations between the beam line and the geometric center of the 4-rod structure were carefully measured.

First, the beam line was defined as the line connecting the two center points of both end flanges. As illustrated in Fig. 17(a), we measured two side surfaces of each electrode and determined symmetrical planes in the horizontal and vertical directions. The interval between the measured

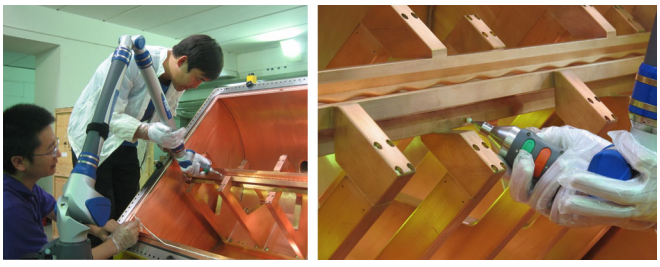

FIG. 16. RFQ mechanical measurements.

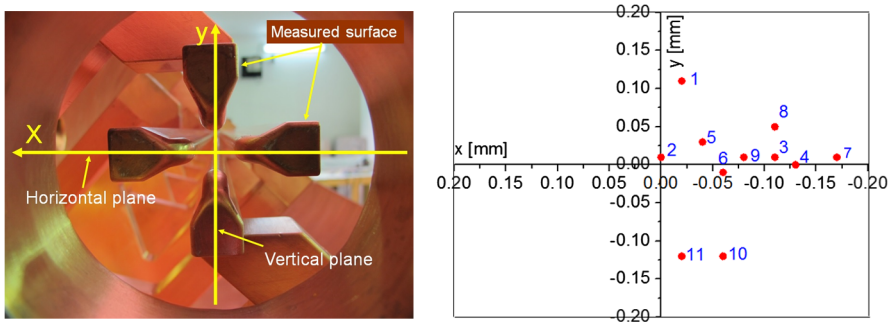

(a) (b)

FIG. 17. The measured surfaces and the deviation results.

points was 20 cm along each electrode. Thus, we obtained a geometric center line from the intersection between the horizontal and vertical planes. Next, we evaluated the coaxial alignment between the geometric center line of the electrodes and the beam axis. The measured maximum and minimum deviations were 0.17 mm and 0.01 mm [as shown in Fig. 17(b)], respectively, and the mean value was 0.07 mm, slightly larger than the design requirement of 0.05 mm. The main reason for this discrepancy may be inaccuracies in the assembly process and the stresses, which were accumulated during manufacturing and assembly, were then released by the vibrations experienced during the long shipping period. Another reason may be the gravity-induced deformation of the electrodes at a 45° rotation. We decided that the shift did not require correction unless the beam test results were unsatisfactory.

C. Rf measurements of RFQ

The low-power rf measurements of the RFQ had two purposes: the first was to measure the rf properties of the cavity after its long transport and assembly, and the second was to evaluate the quality of the electric field generated by the electrodes. Both of these activities were key steps in validating the previous procedures and provided a basis for the subsequent power conditioning.

1. Rf performance of the cavity

First, the frequency in the operating mode and the quality factor Q_0 of the RFQ cavity were measured. The S_{11} parameter of the power coupler was adjusted to −44 dB. The S_{21} parameter of the pickup was adjusted to −49.746 dB. In this critical coupling state, the measured Q_0 value of the cavity was 6440, which is 87.7% of the simulated result with modulation. The initially measured frequency without any tuner inserted was 53.607 MHz, which is only 60 kHz from the operating frequency of 53.667 MHz. We also measured the frequency range of the tuners. The maximum insertion length of each tuner is 40 mm, which results in an increase of 30 kHz. The total 120 kHz increase that can be achieved using all 4 tuners provides a sufficient safety margin to ensure that the RFQ can be tuned to the desired operating frequency. Thus, the additional tuning plates that were designed to be installed on the base plate were deemed unnecessary and will not be used. Generally, the rf performance of the cavity was found to satisfy expectations.

The conventional perturbation method was used to measure the electric field of the RFQ [23,24]. The bead was moved on the symmetric plane of each quadrant in the RFQ, and the three transverse distances from the beam axis to the bead were 10, 15 and 20 mm. At each transverse position, the bead was moved back and forth twice between the entrance and exit of the cavity. During the measurement, the temperature and humidity of the environment were recorded; their values fluctuated in the ranges of 25–28 °C and 30%–50%, respectively.

2. Measurements of the electric field flatness

Based on the analysis presented in Sec. II B 2, the flatness of the field was evaluated from the field distribution normalized with respect to its average strength, and the dipole field was assessed in terms of the field strength ratio between quadrants I and III.

Finally, the flatness of the quadrupole field was calculated by normalizing the averaged fields $E_{i(2,4)}$ and $E_{i(1,3)}$ with respect to their average values of $\bar{E}_{2,4}$ and $\bar{E}_{1,3}$, respectively. These normalized results were used to evaluate the flatness of the field.

Figure 18 shows the flatness of the electric field sampled at positions where the distance to the beam axis was 20 mm in the transverse plane. The solid lines represent the experimental results, whereas the dashed lines represent the simulated results. The red lines denote the average results for quadrants II and IV, and the black lines denote the average results for quadrants I and III. As seen in Fig. 18, the measured flatness of the field is in the range of ±2.5%, indicating that the field distribution satisfies the design requirements presented in Sec. II B.

D. Measurement of the dipole components

Figure 19(a) shows the ratio of the dipole field values sampled at a distances to the beam axis of 20 mm in the

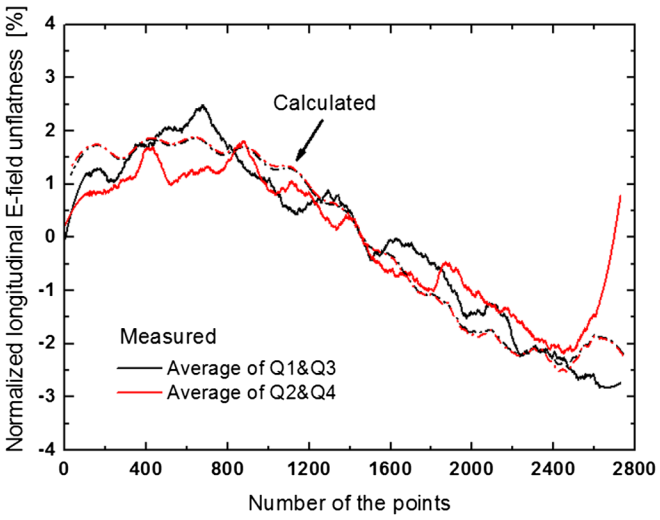

FIG. 18. The longitudinal unflatness of the electric field along the RFQ.

transverse plane. The solid lines represent the experimental results, whereas the dashed lines represent the simulated results. The experimental measurements indicate that the dipole field is lower than 10% in most regions of the electrodes, whereas in some sections, this contribution is in the range of 10%–20%, especially in the high-energy section. These characteristics are of considerable relevance to the installation error of the electrodes, as indicated in the analysis presented in Sec. III B of this paper. The most severe dipole field contribution, reaching a maximum of 12%, was found in the high-energy section, as shown in Fig. 19(a).

Figure 19(b) shows the dipole field components measured at 15 mm and 20 mm from the beam axis. The displacement of the aperture center of the structure is also shown in this figure. As seen in Fig. 19(b), the evolution of the dipole field component is highly correlated with the evolution of the displacement of the center of the electrode aperture. After traveling 1200 mm along the beam axis, the aperture center is shifted to the right with respect to the entering beam, as observed from the results presented in Sec. III B. As a result, the field measured in quadrant I is stronger than that in quadrant III. Subsequently, the dipole field component increases after 1200 mm. Simulations of the beam transport in this extremely nonideal field were performed, and the results show that although the dipole field introduces some oscillation in the beam envelope, the performance is still acceptable.

IV. RF POWER CONDITIONING AND BEAM COMMISSIONING

The experimental setup for the RFQ beam commissioning is depicted in Fig. 20. The beam transport line consisted of an ECR ion source, an LEBT system based on a 90° bending magnet, three solenoids, four matching quadrupoles, and two beam diagnostic systems. One beam diagnostic system, including two movable slits and an emittance scanner, was installed in the region following the bending magnet at about 0.6 m downstream. The other double-slit type emittance scanners, which was used to measure the output emittance of the RFQ, was placed about 0.69 m downstream from the RFQ exit. Three Faraday cups were equipped at various locations along the beam line, and all Faraday cups and slits were water cooled.

In addition, the RFQ was designed to accelerate prebunched beams formed by a MHB, which operates at 13.4167 MHz and its second and third harmonics, to provide a very small longitudinal emittance with total 82.2% injection efficiency [25]. Because the MHB was temporarily unavailable during the on-line installation of the RFQ, the testing was performed using DC ion beams. The RFQ cavity was connected to the 53.667 MHz solid-state rf amplifier through a $3\frac{1}{8}''$ coaxial tube.

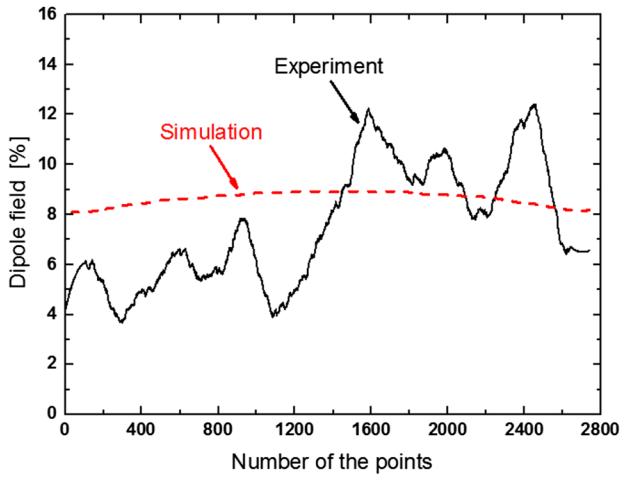

(a)

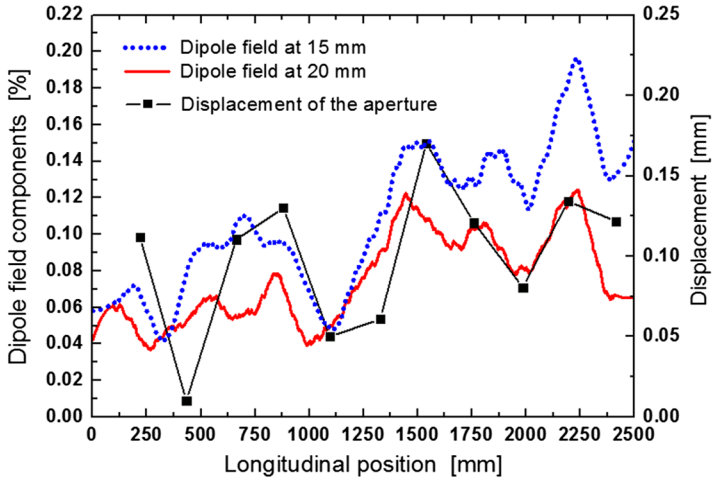

(b)

FIG. 19. The ratio representing the dipole field component.

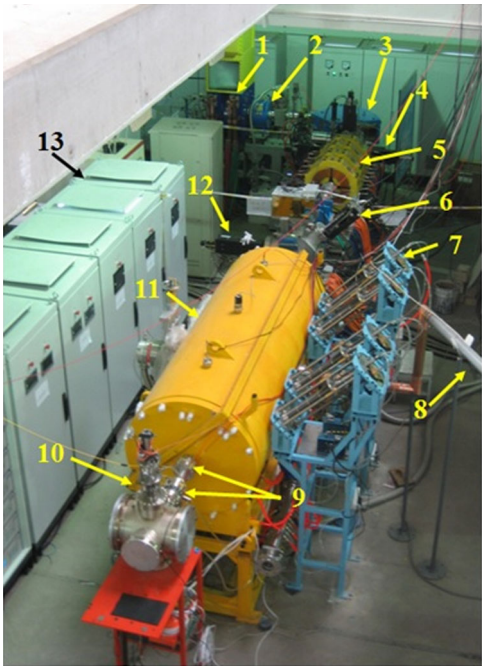

FIG. 20. Overview of the RFQ test area: 1—ECR ion source; 2—solenoid; 3–90° bending magnet; 4—emittance scanner; 5—matching quadrupoles; 6 and 10—movable wire scanner; 7—movable tuner; 8—RF amplifier coaxial tube; 9—fast current transformers (FCTs); 11—RFQ; 12—water-cooled Faraday cups; 13—electric power supply.

A. High-power conditioning

After the rf measurements, the high-power conditioning of the RFQ was performed. The experimental setup is shown in Fig. 21(a). The primary purpose of the tests at high rf power was to check the rf stability of the 4-rod RFQ.

The attenuation power was monitored via the designated pickup loop and measured using an Agilent network analyzer (DS09064A). For safety considerations, four power attenuators (one −30 dB, one −10 dB and two −20 dB) were connected between the network analyzer and the forward loop, backward loop and two pickup loops, respectively. The intervane voltage could be calculated by measuring the rf power from the calibrated pickup loop. For instance, a measured pickup loop power of 1.78 mW would correspond to 50 kV, which is the design voltage for the acceleration of $^{40}Ar^{8+}$ ions from 3.728 keV/u to 143 keV/u. To accelerate ions with a charge-to-mass ratio of 1/7 to the same energy, such as $^{238}U^{34+}$, the measured power should be 3.49 mW, corresponding to the design voltage of 70 kV for this purpose.

The conditioning was begun in pulsed mode at a low rf power, such as 5 kW, with a 5% duty factor under 3.9×10^{-6} Pa vacuum. The input power was then gradually increased by increasing the length and amplitude of the pulse without any serious vacuum troubles. After approximately 40 h of conditioning, 35 kW was fed into the cavity at a duty factor of 30% while maintaining the vacuum below 2.0×10^{-5} Pa [as shown in Fig. 21(b)]. Next, the conditioning procedure was shifted into CW mode. In May 2014, a CW rf power of 35 kW was successfully input. The vacuum and the stability of the frequency were continuously improved. We measured the rate of the frequency shift to be 2.18 kHz/kW when the commissioning power of the cavity had reached 35 kW under CW conditions. The temperature of the output water from each cooling channel was measured and recorded during the rf commissioning. These temperatures did not increase significantly during CW operation. For example, the temperatures of the base plates and stems increased from 19.7 °C to 24.5 °C as the rf power was increased from 0 kW to 35 kW. During the same process, the temperatures of the electrodes were kept below 26 °C. These results indicate that the RFQ cavity possesses good mechanical strength and that the water cooling is effective.

To measure the intervane voltage, a high-purity Ge detector cooled with liquid nitrogen was placed opposite to the lead-glass observation window to measure the X-ray energy spectrum, as shown in Fig. 22(a). The measured Bremsstrahlung spectrum is shown in Fig. 22(b). The red curve represents the fitted Gaussian curve that was used to estimate the intervane voltage. The shunt impedance R of the RFQ was also calculated from the measured results [26].

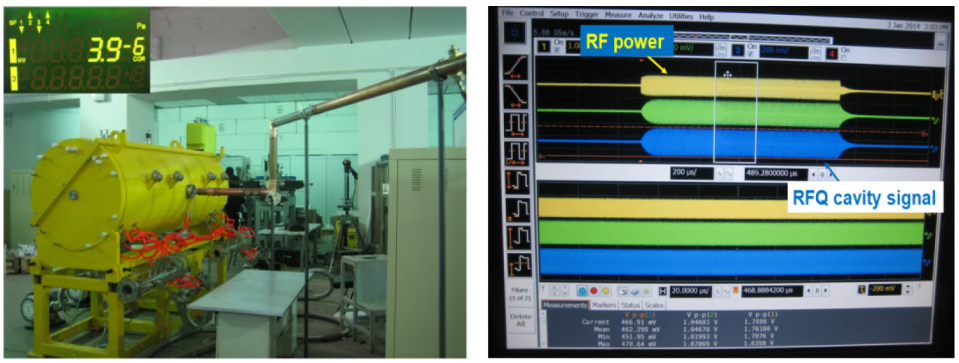

(a) (b)

FIG. 21. High-power testing of the RFQ.

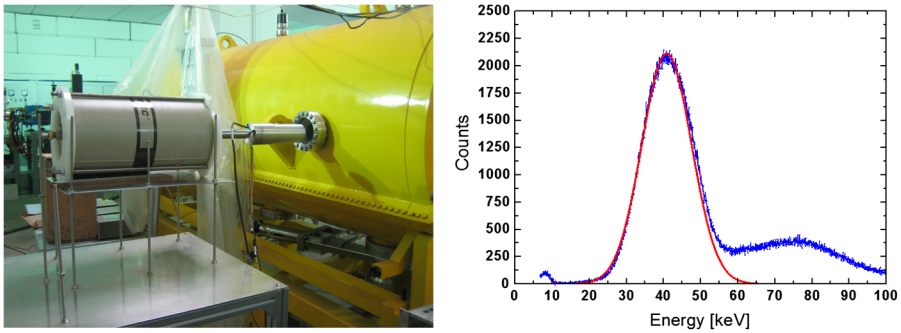

FIG. 22. The setup for the X-ray spectrum measurement.

Based on the analysis of the measured spectrum, we determined that approximately 30 kW is required to generate a 70 kV inter-vane voltage, as shown in Fig. 23. In practice, the real input power must be higher than 30 kW, considering that the measured Q_0 is only 88.2% of the design value. Because the ratio R/Q_0 depends only on the rf structure, the real specific shunt impedance is 352.7 kΩm. Thus, the shunt impedance is 140 kΩ, and the corresponding input power is 35 kW for an ion beam with a mass-to-charge ratio of $A/q = 7$. This result is consistent with the simulation, and the rf properties can be further improved via an advanced power test.

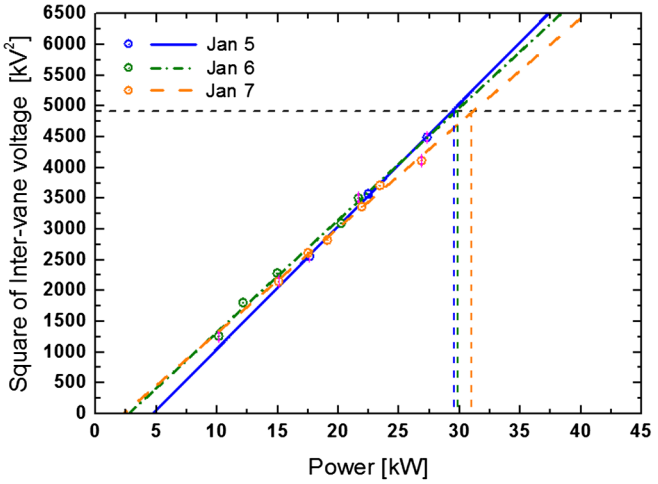

FIG. 23. The calculated inter-vane voltage as a function of rf input power.

B. Beam commissioning

After successful conditioning, RFQ beam commissioning using an $^{40}Ar^{8+}$ ion beam was carefully performed. The design intervane voltage is 10 kV per A/q. Therefore, a voltage of 50 kV was required for the $^{40}Ar^{8+}$ beam test, according to the high-power conditioning results. The rf power required for the acceleration was thus approximately 17.85 kW.

During the on-line beam testing, an $^{40}Ar^{8+}$ ion beam extracted from an ECR ion source was used for RFQ commissioning. The total voltage of the ECR was set to 18 kV to provide the 3.728 keV/u design injection energy. The selected $^{40}Ar^{8+}$ test beam was measured using a 90° analyzing magnets and the diagnostic system downstream of the bending magnet. The width of the slit was set to 0.1 mm. Figure 24 shows a typical $^{40}Ar^{8+}$ emittance measurement acquired using the emittance probe [27]. The measured RMS emittance was 0.07π mm mrad. Four matching quadrupoles and two solenoids were tuned to

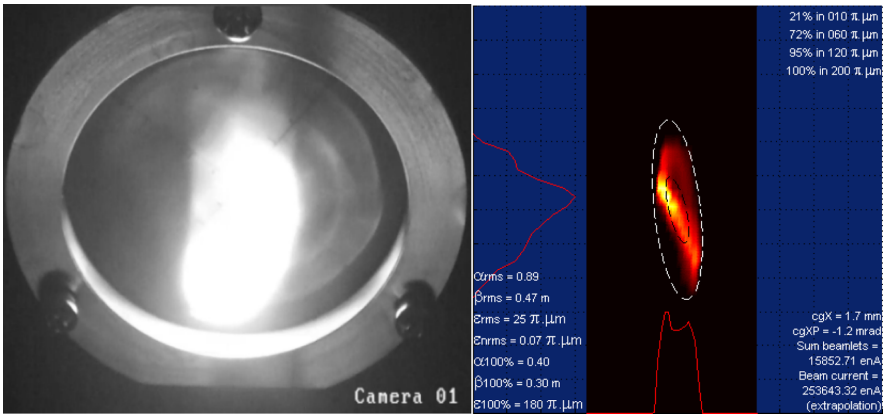

FIG. 24. Emittance measurement after the dipole magnet.

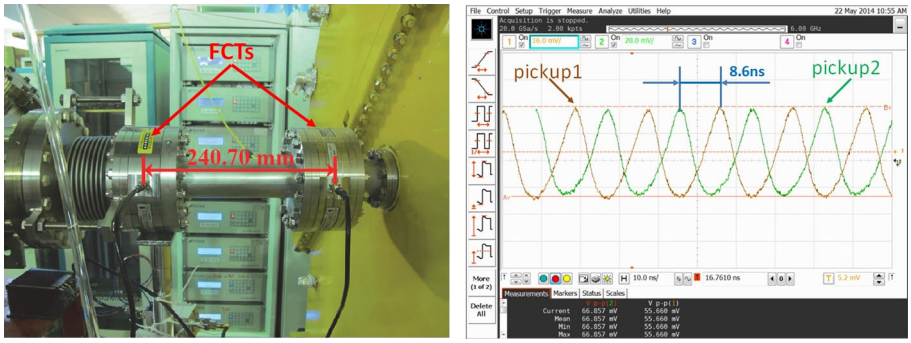

FIG. 25. Beam signals detected by the two FCTs at the RFQ exit.

transport approximately 220 eμA of the $^{40}Ar^{8+}$ ion beam to the RFQ entrance.

The beam energy of the RFQ was measured via the time-of-flight (TOF) method using two fast current transformer (FCTs) installed after the exit of the RFQ. The distance between the two FCTs was 240.7 mm, with a corresponding time of flight of 8.6 ns. Figure 25 shows the beam signals detected by the FCTs. The beam current and transmission were measured using the three Faraday cups upstream and downstream of the RFQ. The measured energy and current were 142.8 keV/u and 198 eμA, respectively.

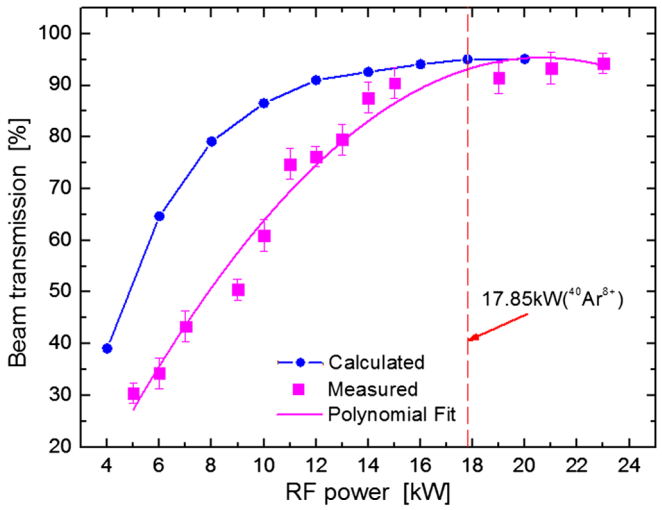

FIG. 26. The measured beam transmission as a function of the rf input power.

The beam transmission through the RFQ as a function of the rf power was also measured, as shown in Fig. 26.

The beam transmission was as high as 94%, consistent with the simulation. The red dashed line represents the design input power of 17.85 kW for $^{40}Ar^{8+}$. The transmission ratio was found to remain nearly constant for an input power greater than 17 kW. Even when the power was decreased to 15 kW, the transmission remained as high as 90%. When the rf power was further decreased, however, the measured transmission decreased sharply compared with the calculated results, which may be explained as follows. The beam may not have been sufficiently focused when the rf power was decreased, resulting in a decrease in the intervane voltage. Moreover, there were no focusing quadrupoles behind the RFQ exit at the time of this measurement. As a result, the beam was scattered in the

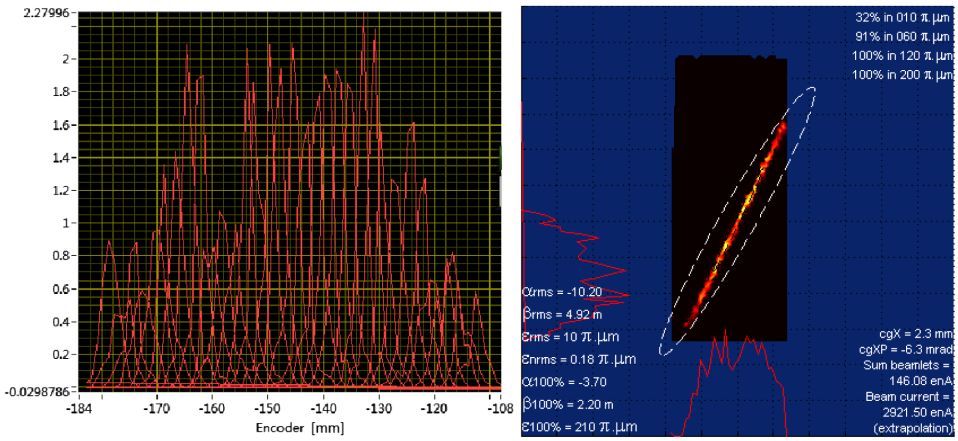

(a) (b)

FIG. 27. The measured beam cross section and horizontal emittance at the exit of RFQ.

vacuum chamber. Many particles escaped the Faraday cups and could no longer be captured. The measured results will be improved by installing a triplet in the MEBT in the near future.

The emittances before and after the RFQ were also measured for 170 μA $^{16}O^{5+}$ beam in July 2015. Figure 27 shows a preliminary measurement results at the diagnostics station 0.69 m downstream of the RFQ exit. The beam distribution in the horizontal plane is shown in Fig 27(a) and the corresponding emittance is shown in Fig 27(b). The measured normalized RMS emittance before and after RFQ are 0.11π mm mrad and 0.18π mm mrad, respectively.

V. SUMMARY AND OUTLOOK

We have designed, fabricated, and performed beam testing on a CW 4-rod RFQ at IMP. Several innovative design concepts and fabrication procedures were implemented in the production of this RFQ. For the beam dynamics design of the RFQ, we increased the transverse phase advance to avoid parametric resonance and adopted a quasi-equipartitioning strategy to control the emittance growth. We also adopted a full 3D approach, including MW-STUDIO and TRACK simulations of the entire structure. These simulations achieved reasonable agreement with the measured results and helped us to validate the design.

Several advanced fabrication technologies were applied for the construction of the RFQ, including precise machining and one-step high-temperature brazing. Precise, high-accuracy measurements were performed throughout the entire manufacturing process. In particular, we developed a new method of checking the installation error of the electrodes in a laboratory environment. This method provides information regarding manufacturing quality. The measured displacement of the electrodes was also confirmed by the results of the rf field measurements. By virtue of the high accuracy of the overall fabrication, the assembly of the RFQ was straightforward and resulted in excellent alignment.

Rf measurements and high-power conditioning yielded experimental results that were in general agreement with the MW-STUDIO simulation. Two kinds of ion beams ($^{40}Ar^{8+}$ and $^{16}O^{5+}$) were used for the commissioning. The beam energy reached 142.8 keV/u, and the transmission was found to be greater than 94% for the $^{40}Ar^{8+}$ ion beam. The emittance at the RFQ exit was also measured preliminary using $^{16}O^{5+}$ ion beam. These initial beam test results are very promising.

In the near future, the accurate measurement of the emittance at the RFQ exit will be performed after the triplet installed in MEBT section. Several beam parameters, such as the energy spread and the acceleration efficiency, will be also carefully measured. Furthermore, high-power conditioning and beam tests using different ions with a higher charge-to-mass ratio are desired.

ACKNOWLEDGMENTS

X. Yin thanks the numerous IMP colleagues who have been involved in this project over the past years. Many thanks to the Peking University collaborators for their cooperation. This work was supported by the National Natural Science Foundation of China under Contracts No. 10635090 and No. 11375243.

[1] J. W. Xia, W. L. Zhan, B. W. Wei *et al.*, Nucl. Instrum. Methods Phys. Res., Sect. A **488**, 11 (2002).
[2] Y. He, Z. J. Wang, C. Xiao *et al.*, in *Proceedings of the 25th International Linear Accelerator Conference, LINAC-2010, Tsukuba, Japan* (KEK, Tsukuba, Japan, 2010), p. 482.
[3] X. Yin, Y. Yuan, and X. Zhang *et al.*, in *Proceedings of the 5th International Particle Accelerator Conference (IPAC'14), Dresden, Germany* (2014), p. 1658.
[4] G. Liu, Y. R. Lu, and Z. Wang *et al.*, in *Proceedings of the 3rd International Particle Accelerator Conference, New Orleans, LA, 2012* (IEEE, Piscataway, NJ, 2012), p. THPPP041.
[5] G. Liu, Y. R. Lu, Z. Wang *et al.*, Nucl. Instrum. Methods Phys. Res., Sect. A **701**, 186 (2013).
[6] K. R. Crandall, T. P. Wangler, L. M. Young *et al.*, Report No. LA-UR-96-1836, 2005.
[7] R. H. Stokes, K. R. Crandall, J. E. Stovall, and D. A. Swenson, in *Proceedings of the 1979 Particle Accelerator Conference, San Francisco, CA* (1979), pp. 3469–3471.
[8] Y. Kondo, K. Hasegawa, and T. Morishita, Phys. Rev. ST Accel. Beams **15**, 080101 (2012).
[9] K. R. Crandall, R. H. Stokes, and T. P. Wangler, in *Proceedings of LINAC79, Montauk, New York* (1979), BNL 51134, p. 205–216.
[10] M. Reiser, *AIP Conf. Proc.* 346, 364 (1995).
[11] P. Lapostolle and M. Weiss, Report No. CERN-PS-2000-001 (DR), 2000.
[12] M. Reiser, *Theory and Design of Charged Particle Beams* (Wiley, New York, 1994).
[13] R. A. Jameson, *AIP Conf. Proc.* 279, 969 (1992).
[14] X. Q. Yan, R. A. Jameson, Y. R. Lu, Z. Y. Guo, J. X. Fang, and J. E. Chen, Nucl. Instrum. Methods Phys. Res., Sect. A **577**, 402 (2007).
[15] M. Reiser and N. Brown, AIP Conf. Proc. **377**, 329 (1996).
[16] I. Hofmann, in *Proceedings of the Particle Accelerator Conference, Vancouver, BC, Canada, 1997* (IEEE, New York, 1997).
[17] I. Hofmann, G. Franchetti, O. Boine-Frankenheim, J. Qiang, and R. D. Ryne, Phys. Rev. ST Accel. Beams **6**, 024202 (2003).
[18] I. Hofmann, Phys. Rev. ST Accel. Beams **16**,084201 (2013).
[19] http://www.phy.anl.gov/atlas/TRACK.
[20] B. Mustapha, A. A. Kolomiets, and P. N. Ostroumov, Phys. Rev. ST Accel. Beams **16**,120101 (2013).
[21] http://www.cst.com/.

[22] M. Okamura, J. Alessi, E. Beebe *et al.*, in *Proceedings of the 25th International Linear Accelerator Conference, LINAC-2010, Tsukuba, Japan* (KEK, Tsukuba, Japan, 2010), p. 473.
[23] R. G. Carter, IEEE Trans. Microwave Theory Tech. **49**, 918, 2001.
[24] H. Klein, in CERN Report No. CERN 92-03, 1992.
[25] P. N. Ostroumov *et al.*, Phys. Rev. ST Accel. Beams **15**,110101 (2012).
[26] K. B. Mallory, J. Appl. Phys. **29**, 790, 1958.
[27] W. Lu, L. T. Sun, C. Qian *et al.*, Rev. Sci. Instrum. **86**, 043301 (2015).